NANO LETTERS

Letter

pubs.acs.org/NanoLett

Bandgap, Mid-Gap States, and Gating Effects in MoS_2

Chih-Pin Lu,[‡,†] Guohong Li,[†] Jinhai Mao,[†] Li-Min Wang,[‡] and Eva Y. Andrei*[,†]

[†]Department of Physics and Astronomy, Rutgers University, Piscataway, New Jersey 08855, United States

[‡]Department of Physics, National Taiwan University, Taipei, 10617 Taiwan, Republic of China

Supporting Information

ABSTRACT: The discovery of graphene has put the spotlight on other layered materials including transition metal dichalcogenites (TMD) as building blocks for novel heterostructures assembled from stacked atomic layers. Molybdenum disulfide, MoS_2, a semiconductor in the TMD family, with its remarkable thermal and chemical stability and high mobility, has emerged as a promising candidate for postsilicon applications such as switching, photonics, and flexible electronics. Because these rely on controlling the position of the Fermi energy (E_F), it is crucial to understand its dependence on doping and gating. To elucidate these questions we carried out gated scanning tunneling microscopy (STM) and spectroscopy (STS) measurements and compared them with transport measurements in a field effect transistor (FET) device configuration. This made it possible to measure the bandgap and the position of E_F in MoS_2 and to track its evolution with gate voltage. For bulk samples, the measured bandgap (~1.3 eV) is comparable to the value obtained by photoluminescence, and the position of E_F (~0.35 eV) below the conduction band, is consistent with N-doping reported in this material. We show that the N-doping in bulk samples can be attributed to S vacancies. In contrast, the significantly higher N-doping observed in thin MoS_2 films deposited on SiO_2 is dominated by charge traps at the sample−substrate interface.

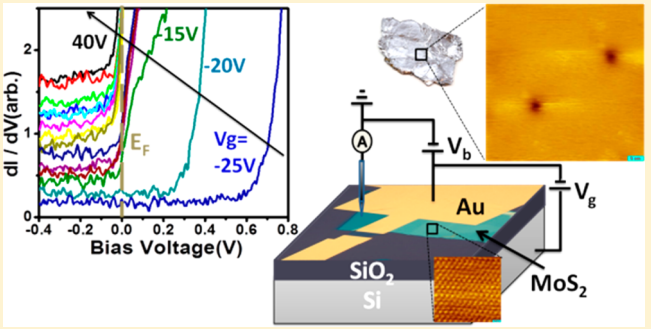

KEYWORDS: *MoS_2, scanning tunneling microscopy/spectroscopy, two-dimensional electronics, defects, atomic resolution imaging*

The development of techniques to isolate atomic layers[1] and to integrate them into atomically precise heterostructures[2] has enabled the design of novel material properties and applications by exploiting the proximity between layers with different electronic structures such as conducting (graphene), insulating (hBN), and semiconducting (2H-MoS_2).[3−6] 2H-MoS_2, a layered material in the transition metal dichalcogenite family has recently attracted much attention owing to its remarkable electrical and optical properties. Bulk MoS_2 has an indirect bandgap of 1.2−1.3 eV[7−10] which, due to quantum confinement, crosses over to a direct bandgap of ~1.9 eV when the material is exfoliated down to a monolayer.[11] Thin layers of MoS_2 are well suited as a channel material in FET applications exhibiting high room temperature mobility, almost ideal switching characteristics, and low standby power dissipation.[6,12−14] Furthermore, the absence of dangling bonds and of surface states and its resistance to oxidation make MoS_2 a particularly good candidate for STM studies. In both bulk and thin layers of MoS_2 deposited on SiO_2 the conductivity consistently exhibits n-type character,[6,15−17] but to date, the source of the N-doping remains unclear. Proposals include substitutional impurities[14,18] such as Cl, Br or Re,[19] S vacancies,[20−22] and impurities trapped at the interface with the SiO_2 substrate.[3,23] Here, we employ STM/STS combined with transport measurements to elucidate the nature of doping in MoS_2 and its connection to the switching characteristics of the thin layers.

Samples were prepared by exfoliating bulk 2H-MoS_2 crystals (purchased from SPI) onto SiO_2 (300 nm)/Si substrates to achieve the desired sample thickness and to expose a fresh sample surface. MoS_2 flakes were identified by optical microscopy and subsequently characterized by atomic force microscopy (AFM) and Raman spectroscopy in ambient conditions. The AFM height profile of one of the samples, shown in Figure 1a, indicates a thickness of 4.2 nm corresponding to six layers. The Raman spectra, Figure 1b, for single, multilayer, and bulk MoS_2 samples show a monotonic evolution with the number of layers.[24] For the six-layer sample the spectrum is already very close to that of bulk. FET devices were fabricated using e-beam lithography with Ti/Au (2 nm/60 nm) contacts deposited by electron-beam evaporation at a base pressure of 2×10^{-7} Torr. Prior to measurements the MoS_2 devices were baked for 3 h in forming gas (90% Ar, 10% H_2) at 230 °C. STM and STS measurements were performed at 80 K in a home-built STM[25−27] using mechanically cut Pt−Ir tips. The STM images were recorded in constant current mode with the bias voltage, V_b, applied to the sample, whereas the STM tip was held at ground potential. The differential conductance (dI/dV) spectra were measured using a

Received: May 6, 2014
Revised: June 26, 2014

   dx.doi.org/10.1021/nl501659n | *Nano Lett.* XXXX, XXX, XXX−XXX

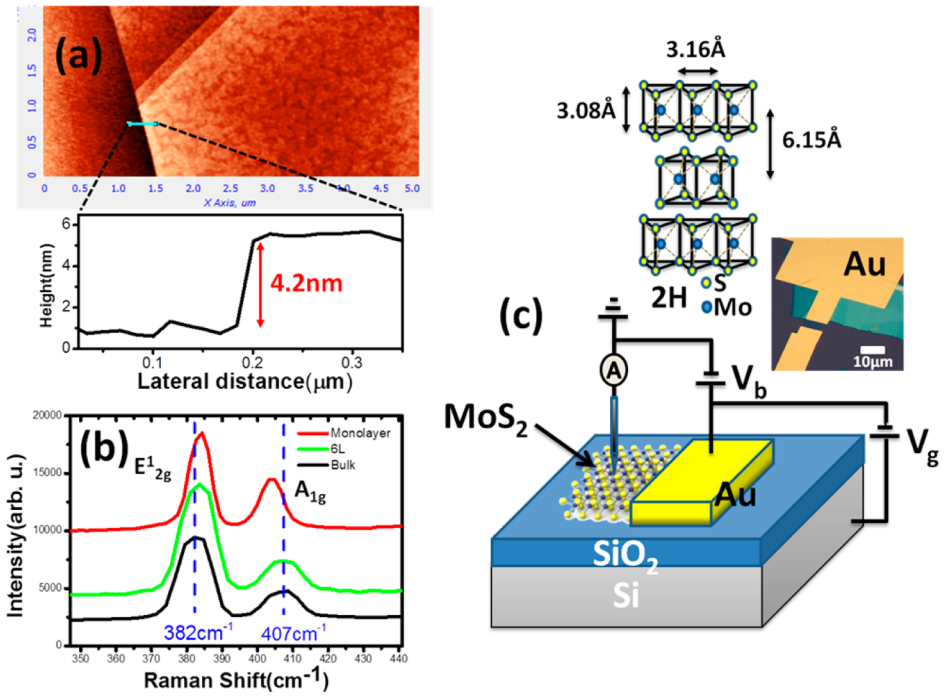

Figure 1. (a) AFM image of multilayer MoS_2 on a SiO_2/Si substrate. The step height indicates a thickness of 4.2 nm corresponding to six layers. (b) Raman spectrum showing the in-plane E^1_{2g} and out-of-plane A_{1g} resonances of single, multilayer, and bulk MoS_2. The laser wavelength was 633 nm and the spot size ~2 μm. (c) Schematic of MoS_2 sample mounted in an STM configuration with gating capabilities. The sample bias V_b is applied between the STM tip and the MoS_2 sample contacted by a Ti/Au electrode. The back gate voltage V_g is applied between the P-doped Si substrate and the top electrode. Inset: Optical micrograph of a mechanically exfoliated multilayer MoS_2 flake and schematics of the atomic structure of 2H-MoS_2.

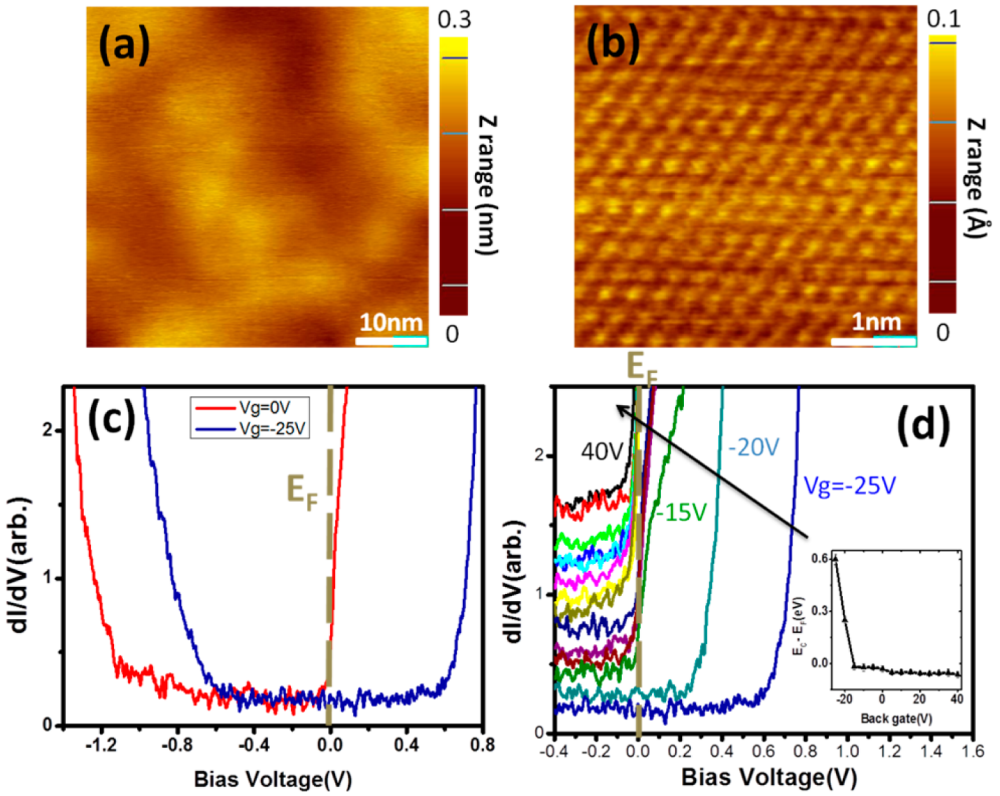

Figure 2. (a) STM constant current topography image of a six-layer MoS_2 sample measured in the device configuration of Figure 1c for V_b = 1.4 V and I = 20 pA. (b) Same as (a), zooming in to atomic resolution. (c) dI/dV spectrum taken in the area shown in (b) for V_g = 0 V (red) and V_g = −25 V (blue) (d) Evolution of dI/dV spectrum with V_g. Curves are offset vertically and only show the CB edge. Inset: Gate voltage dependence of the position of the Fermi energy relative to the bottom of the conduction band.

dx.doi.org/10.1021/nl501659n | *Nano Lett.* XXXX, XXX, XXX−XXX

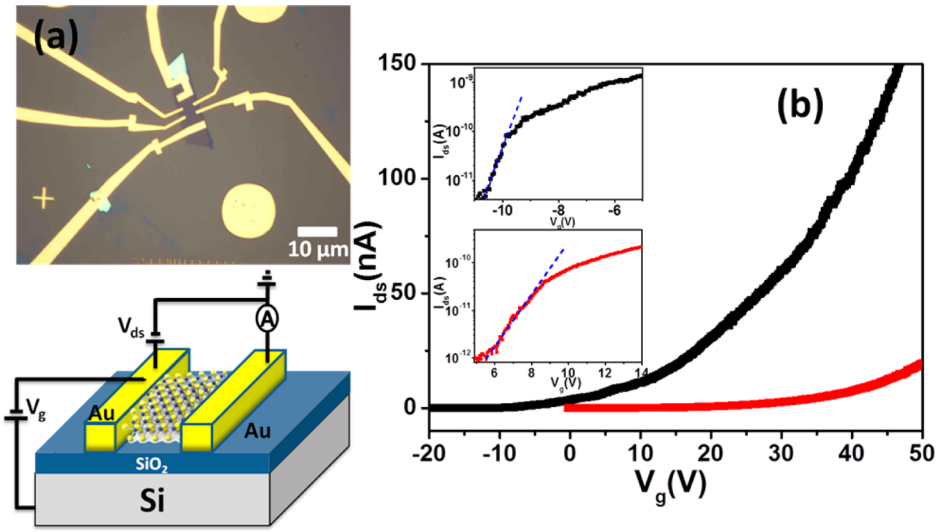

Figure 3. (a) Top: Optical micrograph of a thin MoS_2 device supported on a 300-nm-thick SiO_2 substrate configured for a 2-terminal transport measurements. Bottom: Schematic of the MoS_2 FET device. (b) Evolution of source-drain current, I_{ds}, with V_g at 300 K and V_{ds} = 0.1 V for the device shown in (a). The red and black curves correspond to measurements before and after annealing, respectively. Inset: same data on a semilogarithmic scale.

lock-in technique (ac modulation: 5 mV_{rms} at 440 Hz) with fixed tip to sample distance. Gated STS measurements were carried out in a device configuration, shown in Figure 1c, in which a thin sample was deposited on a 300 nm SiO_2 substrate capping a degenerately P-doped Si gate.

To investigate the source of doping in thin MoS_2 samples, we employed a six-layer sample configured in an FET device, which combines STS with gating capability. As shown in the STM topography image in Figure 2a, the sample surface is relatively flat and clean with corrugations not exceeding ~0.2 nm over a 50 × 50 nm area. Zooming in to atomic resolution in Figure 2b reveals the sulfur surface atoms arranged in a triangular lattice with lattice constant ~0.31 nm, in agreement with the accepted crystallographic value, of 0.316 nm. This indicates high surface quality with no surface contamination left over from the fabrication process. STS measurements at the same position revealed a bandgap of 1.31 ± 0.06 eV (Figure 2c and Supporting Information S1) that is comparable to the photoluminescence gap in similar samples (Supporting Information S2) and in earlier reports,[10] suggesting that tip induced band-bending does not significantly affect our measurements.[28] Using the setup shown in Figure 1c we studied the local electronic properties as a function of gate voltage (V_g) across the SiO_2 substrate. For V_g = 0 V, E_F is at the edge of the conduction band (CB), indicating the presence of shallow donors, which is in agreement with previous reports of unintentional N-doping of such devices.[3,6] A positive V_g slowly pushes E_F into the CB (Figure 2d), reflecting the high density of states near the bottom of the CB. In contrast, a negative V_g moves E_F away from the CB, making the sample less conductive. The effect of negative gating suddenly accelerates at a threshold voltage $V_{gt} \sim -15$ V as shown in Figure 2d. Applying $V_g = -25$ V shifts the position of E_F to the center of the bandgap, as shown in Figure 2c. In this regime, where the tunneling current is negligibly small, special care was taken to avoid crashing the tip and damaging the sample, as described in the Supporting Information S3.

From the evolution of E_F with V_g in the gap region (inset in Figure 2d), we estimate $dE_F/dV_g = 0.06q$, where q is the magnitude of the electron charge. Rewriting this expression in terms of the quantum capacitance,[29] $C_Q = q^2((dn)/(dE_F))$, where n is the carrier density per unit area, we obtain $((dE_F)/(dV_g)) = 1/q((dE_F)/(dn))((dqn)/(dV_g)) = qC/(C_Q)$. Noting that $((dqn)/(dV_g)) = C = (1/(C_{ox}) + 1/(C_Q))^{-1}$ is the total device capacitance resulting from the series connection of C_Q with the oxide capacitance, $C_{ox} = \varepsilon_{ox}/d_{ox} \approx 12$ nF·cm^{-2}, and rewriting $((dE_F)/(dV_g)) = 0.06q = qC/(C_Q)$, we find $C_Q/C_{ox} = 15.6$. This gives $C_Q = 187$ nF·cm^{-2}, $C = 11.3$ nF·cm^{-2} for our device. From the quantum capacitance, we can obtain the total density of states per unit area: $((dn)/(dE_F)) \equiv D(E_F) \sim 1.16 \times 10^{12}$ states/eV cm^{-2}. We next compare the STS results to transport measurements of a thin sample in an FET device configuration.

In order to correlate the STS data with transport measurements, we used a two-terminal device configuration shown in Figure 3 to follow the gate dependence of the drain source current, I_{ds} (V_g) in four samples (Supporting Information S4). We found that the device characteristics such as mobility and subthreshold slope improve substantially after *in situ* annealing in vacuum (10^{-6} mbar) at 120 °C for 20 h, similar to results reported in the literature.[3] For the bilayer sample shown in Figure 3b, the conduction threshold, initially V_{gt} = 8 V, decreased after annealing to $V_{gt} = -10$ V approaching the value obtained by STS. From the measured gate dependence, we obtain the field-effect mobility at 300 K, $\mu = (L/(WC_{ox}))(1/(V_{ds}))(dI_{ds}/dV_g) \sim 3$ cm^2 V^{-1} s^{-1}, which increased to ~6 cm^2 V^{-1} s^{-1} after annealing. Here, L = 7.4 μm, W = 6.5 μm are the channel length and width, respectively. The observed monotonic increase of the postanneal mobility with number of layers (Supporting Information S4) suggests that scattering from surface defects plays an important role. Another important metric of device quality is the subthreshold swing[30] defined as $S = (\ln 10)k_BT/q\ (1 + C_Q/C_{ox})$. The subthreshold swing, which can also be expressed as $S = (dV_g/(d(\log I_{ds})))$, characterizes the switching time of the device: the lower the S, the faster the device. Its value can be obtained from $I_{ds}(V_g)$, by measuring the subthreshold slope: $((d(\log I_{ds}))/(dV_g))$. For $C_Q \ll C_{ox}$, the device reaches its thermodynami-

dx.doi.org/10.1021/nl501659n | Nano Lett. XXXX, XXX, XXX−XXX

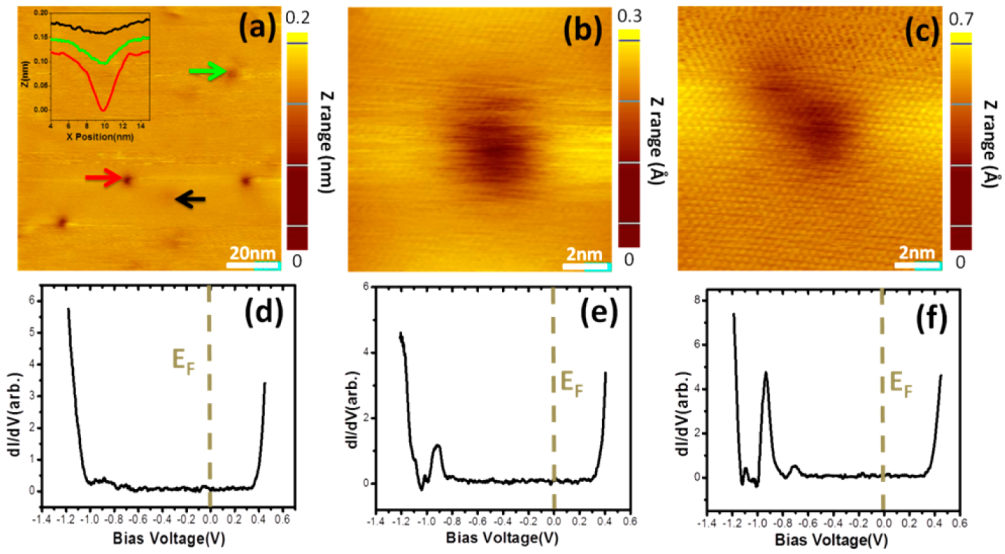

Figure 4. (a) STM constant current topography image of a 50 × 50 nm area at V_b = 1.4 V and I = 20 pA on bulk MoS_2 showing three types of defects with different apparent depths as indicated by the height profiles in the inset. (b) Constant current STM image on an isolated defects. (V_b = 1.2 V and I = 20 pA). (c) Constant current STM atomic resolution image on a twin-defect. (V_b = 1.2 V and I = 20 pA). (d) dI/dV spectrum taken far from any defect. (e) dI/dV spectrum on isolated defect in (b) shows a pronounced in-gap resonance near −0.94 V. The Fermi level is ∼0.35 eV below the CB edge. The measurement was referenced to a set-point with tunneling resistance 15 GΩ (bias voltage V_b = −1.5 V and tunneling current I = 100 pA). (f) dI/dV spectrum on the twin-defect in (c) shows a pronounced in-gap resonance near −0.94 V and a satellite peak at −0.7 V. Parameters are the same as in (e).

cally limited fastest performance with $S_{min} = (\ln 10)k_BT/q$ = 60 mV/decade at T = 300 K. This is significantly below the S values measured in our devices indicating that they operate in the opposite limit $C_Q \gg C_{ox}$. For the sample discussed here, S = 1.5 V/decade at T = 300 K prior to annealing, gives an estimated C_Q ∼288 nF cm^{-2} ≫ C_{ox}. The device improved after annealing dropping to S = 0.7 V/decade, and C_Q ∼128 nF cm^{-2}. Remarkably, the values of C_Q obtained by transport agree with the STS values within the experimental uncertainty, indicating that transport measurements can provide a reliable measure of the quantum capacitance.

The weak thickness dependence of the postanneal to preanneal ratio of S together with the monotonic increase of the postanneal mobility with layer number (Supporting Information S4), suggests that surface traps at the SiO_2 interface significantly contribute to the N-doping observed in these devices. In order to trace the origin of the doping and to establish whether it is due to bulk or surface traps, we carried out STM/STS on a freshly cleaved bulk sample whose surface has not undergone wet treatment and that is not supported by a SiO_2 substrate. The sample was mounted into the STM head using silver paint to attach the back of the sample to a reference electrode. STS measurements on the bulk sample reveal a band gap of ∼1.29 ± 0.05 eV (Supporting Information S1), Figure 4d, consistent with the photoluminescence results. Contrary to the results in the thin sample, E_F is now ∼0.35 eV below the CB indicating the presence of deep donors. Indeed large area (50 × 50 nm) STM topography, shown in Figure 4a, which was obtained at V_b = 1.2 V reveals defects as dark spots. Three types of defects can be distinguished by their apparent depth and diameter: darkest (−0.12 nm in depth and 3 nm in diameter); intermediate (−0.05 and 4 nm); faint (−0.02 and 5.5 nm). Zooming into the defects to resolve the atomic structure, we find that the lattice periodicity is intact suggesting that the defects are buried under the surface (Supporting Information S5, S6). According to *ab initio* calculations, the electronic structure of point defects on the surface of MoS_2 are tightly localized within one atomic distance.[19] By contrast, the defects observed here are extended several lattice spacings without a localized feature on the central atom. This again indicates defects buried under the surface, similar to the case of buried Mn impurities in GaAs or InAs, which produce a topography signature extending over several lattice spacing.[31−33] Among the reported substitution atoms in MoS_2, only Cl, Br, and Re are consistent with N-doping. However, the ionization energy of these donors, ∼0.16, 0.26, and 0.06 eV respectively,[18,19] is too low to account for the observed E_F ∼ 0.35 eV below the CB. Furthermore, X-ray fluorescence (XRF) and X-ray photoelectron spectroscopy (XPS) analysis of our crystal indicated that, within the experimental resolution of 100 ppm, these elements were not present. As we show next the observed defects are consistent with S vacancies.

Zooming into the center of a defect, Figure 4e and f, the STS spectra reveal a sharp in-gap peak at V_b = −0.94 V that is close to the valence band and not near the CB edge where donor states are expected. This apparent discrepancy reflects the tip-induced band bending.[28] When the bias voltage corresponds to the flat band condition the donor state crosses E_F creating a new conduction path where donor electrons tunnel into empty states of the STM tip which gives rise to a peak in the differential conductance. We can calculate the donor ionization energy, E_d, from the flat band condition: $qV_{FB} = E_A + (E_d)/2 - \Phi_{tip}$, where V_{FB} = −0.94 eV the flat-band bias voltage, E_A = 4.2 eV the electron affinity in MoS_2,[34,35] and Φ_{tip} the work function of the tip. Using the value[36] Φ_{tip} = 5.5 eV for the Pt−Ir tip, we obtain E_d ∼ 0.7 eV below the CB consistent with the position of E_F and with the calculated values for S vacancies.[18−22] This gives an estimate of the defect size:[32] $R \sim \hbar/((2m^*E_d)^{1/2})$ = 0.3 nm (m^* = 0.4m_e is the effective electron mass) which agrees with the calculated size of an S vacancy.[19] However, when buried under the surface, point defects produce a more extended topography image which

dx.doi.org/10.1021/nl501659n | *Nano Lett.* XXXX, XXX, XXX−XXX

typically increases with the depth,[31−33] consistent with the fact that the atomic topography image shows no missing surface atoms (Supporting Information S5) (Figure 4c). The three defect sizes can be understood in terms of vacancies located in different S layers underneath the surface.[32,33] In Figure 4c, we show the topography of two almost overlapping features, one stronger than the other, which we attribute to twin-vacancies located in different layers. The STS data measured in the center of the stronger feature, Figure 4f, exhibits a small satellite peak at $V_b = -0.7$ V. Such satellite peaks introduced by twin-defects were reported in earlier STM/STS measurements in semiconductors[32] and attributed to a bonding and antibonding states resulting from the hybridization between the defect states.

To estimate the density of vacancies we measure the surface density of defects of equal size, $N_l \approx 3.5 \times 10^{10}$ cm^{-2}, and assuming the same defect density in all S layers, we obtain the volume density: $N_{3d} = N_l/a \approx 1.1 \times 10^{18}$ cm^{-3}, where $a = 0.31$ nm is the vertical separation between sulfur layers (Supporting Information S7). At room temperature, this gives an activated bulk carrier density of $n \sim N_{3d}e^{-(E_F-E_D)/k_BT} \approx 10^{13}$ cm^{-3} in the ungated devices. We can now estimate the equivalent areal density of activated carriers in the double layer, $t \sim 2.5$ nm, used in the FET device above to be $n_0 = nt \sim 2.5 \times 10^4$ cm^{-2}, which is significantly lower than the measured residual density in thin devices. These results clearly exclude bulk mechanisms, such as substitutional dopants or sulfur vacancies, as the source of the postanneal doping observed in thin layer MoS_2. We must conclude that the N-doping in the thin layer is due to trapped charges at the interface with the SiO_2 substrate, consistent with the observed variability in device quality, with the postanneal decrease in S,[3,23] and with the monotonic increase of postanneal mobility with layer number. Likely candidates for the trapped charges could be Na ions which are notoriously prone to contaminate[37] the surface of SiO_2. For example, in the case of graphene deposited on SiO_2, it is well known that trapped Na ions at the interface cause significant levels of unintentional doping; however, there, Na produces holes, whereas in MoS_2, it induces electron doping.[23,38]

In summary, by combining gated STM and STS together with transport measurements, we have traced the intrinsic N-doping in bulk 2H-MoS_2 to point defects which are consistent with S vacancies. Within the experimental error, we found no evidence of Cl, Br, or Re dopants. Furthermore, we demonstrated that the significantly higher N-doping observed in thin films deposited on SiO_2 is extrinsic and can be attributed to trapped donors at the interface with the SiO_2 substrate.

■ ASSOCIATED CONTENT

Ⓢ Supporting Information

Detailed information is provided on: band gap measurements; photoluminescence measurements; gated STS measurements; MoS_2 FET device performance; atomic resolution topography of defects in 2H-MoS_2; topography of defects seen on the surface of bare and graphene covered 2H-MoS_2; concentration of defects. This material is available free of charge via the Internet at http://pubs.acs.org.

■ AUTHOR INFORMATION

Corresponding Author

*E-mail: eandrei@physics.rutgers.edu.

Notes

The authors declare no competing financial interest.

■ ACKNOWLEDGMENTS

Funding was provided by DOE-FG02-99ER45742 (E.Y.A., G.L, J.M.) and NSF DMR 1207108 (E.Y.A., C.P.L.). We thank F.I.B. Williams, D. Vanderbilt, J. Sofo, F. Guinea, E. Garfunkel, and R.A. Bartynski for useful discussions. We are grateful to S. Rangan, R. Thorpe, and G. Hall for X-ray characterization.

■ REFERENCES

(1) Novoselov, K. S.; Jiang, D.; Schedin, F.; Booth, T. J.; Khotkevich, V. V.; Morozov, S. V.; Geim, A. K. *Proc. Natl. Acad. Sci. U. S. A.* **2005**, *102*, 10451.
(2) Geim, A. K.; Grigorieva, I. V. *Nature* **2013**, *499* (7459), 419−25.
(3) Ayari, A.; Cobas, E.; Ogundadegbe, O.; Fuhrer, M. S. *J. Appl. Phys.* **2007**, *101* (1), 014507.
(4) Wang, Q. H.; Kalantar-Zadeh, K.; Kis, A.; Coleman, J. N.; Strano, M. S. *Nature Nanotechnol.* **2012**, *7*, 699−712.
(5) Chhowalla, M.; Shin, H. S.; Eda, G.; Li, L.-J.; Loh, K. P.; Zhang, H. *Nat. Chem.* **2013**, *5*, 263−275.
(6) Radisavljevic, B.; Radenovic, A.; Brivio, J.; Giacometti, V.; Kis, A. *Nature Nanotechnol.* **2011**, *6*, 147−150.
(7) Kam, K. K.; Parkinson, B. A. *J. Phys. Chem.* **1982**, *86* (4), 463−467.
(8) Ho, W. K.; Yu, J. C.; Lin, J.; Yu, J. G.; Li, P. S. *Langmuir* **2004**, *20* (14), 5865−5869.
(9) Gourmelon, E.; Lignier, O.; Hadouda, H.; Couturier, G.; Bernede, J. C.; Tedd, J.; Pouzet, J.; Salardenne, J. *Sol. Energy Mater. Sol. Cells* **1997**, *46* (2), 115−121.
(10) Mak, K. F.; Shan, J.; Heinz, T. F. *Phys. Rev. Lett.* **2010**, *104* (17), 176404.
(11) Splendiani, A.; Sun, L.; Zhang, Y. B.; Li, T. S.; Kim, J.; Chim, C. Y.; Galli, G.; Wang, F. *Nano Lett.* **2010**, *10* (4), 1271−1275.
(12) Wang, H.; Yu, L. L.; Lee, Y. H.; Shi, Y. M.; Hsu, A.; Chin, M. L.; Li, L. J.; Dubey, M.; Kong, J.; Palacios, T. *Nano Lett.* **2012**, *12* (9), 4674−4680.
(13) Li, H.; Yin, Z. Y.; He, Q. Y.; Li, H.; Huang, X.; Lu, G.; Fam, D. W. H.; Tok, A. I. Y.; Zhang, Q.; Zhang, H. *Small* **2012**, *8* (1), 63−67.
(14) Yin, Z. Y.; Li, H.; Li, H.; Jiang, L.; Shi, Y. M.; Sun, Y. H.; Lu, G.; Zhang, Q.; Chen, X. D.; Zhang, H. *ACS Nano* **2012**, *6* (1), 74−80.
(15) Radisavljevic, B.; Kis, A. *Nature Nanotechnol.* **2013**, *12*, 815−820.
(16) Kim, S.; Konar, A.; Hwang, W. S.; Lee, J. H.; Lee, J.; Yang, J.; Jung, C.; Kim, H.; Yoo, J. B.; Choi, J. Y.; Jin, Y. W.; Lee, S. Y.; Jena, D.; Choi, W.; Kim, K. *Nat. Commun.* **2012**, 3.
(17) Baugher, B. W. H.; Churchill, H. O. H.; Yang, Y. F.; Jarillo-Herrero, P. *Nano Lett.* **2013**, *13* (9), 4212−4216.
(18) Carvalho, A.; Neto, A. H. C. *Phys. Rev. B* **2014**, *89* (8), 081406.
(19) Noh, J.-Y.; Park, M.; Kim, Y.-S.; Kim, H. *arXiv.org e-Print Archive* **2013**, No. http://arxiv.org/pdf/1307.3813.pdf.
(20) Fuhr, J. D.; Saul, A.; Sofo, J. O. *Phys. Rev. Lett.* **2004**, *92*, 026802.
(21) Kim, B. H.; Park, M.; Lee, M.; Baek, S. J.; Jeong, H. Y.; Choi, M.; Chang, S. J.; Hong, W. G.; Kim, T. K.; Moon, H. R.; Park, Y. W.; Park, N.; Jun, Y. *RSC Adv.* **2013**, *3* (40), 18424−18429.
(22) Qiu, H.; Xu, T.; Wang, Z.; Ren, W.; Nan, H.; Ni, Z.; Chen, Q.; Yuan, S.; Miao, F.; Song, F.; Long, G.; Shi, Y.; Sun, L.; Wang, J.; Wang, X. *Nat. Commun.* **2013**, 4.
(23) Dolui, K.; Rungger, I.; Sanvito, S. *Phys. Rev. B* **2013**, *87*, 165402.
(24) Lee, C.; Yan, H.; Brus, L. E.; Heinz, T. F.; Hone, J.; Ryu, S. *ACS Nano* **2010**, *4* (5), 2695−2700.
(25) Li, G.; Andrei, E. Y. *Nat. Phys.* **2007**, *3* (9), 623−627.
(26) Luican, A.; Li, G.; Andrei, E. Y. *Solid State Commun.* **2009**, *149* (27−28), 1151−1156.
(27) Andrei, E. Y.; Li, G.; Du, X. *Rep. Prog. Phys.* **2012**, *75*, 056501.
(28) Feenstra, R. M. *Phys. Rev. B* **1994**, *50* (7), 4561−4570.
(29) Luryi, S. *Appl. Phys. Lett.* **988**, *52* (6), 501−503.

(30) Sze, S. M. *Physics of Semiconductor Devices*, 2nd ed.; Wiley: Weinheim, Germany, 1981.
(31) Loth, S.; Wenderoth, M.; Winking, L.; Ulbrich, R. G.; Malzer, S.; Dohler, G. H. *Phys. Rev. Lett.* **2006**, *96* (6), 066403.
(32) Kitchen, D.; Richardella, A.; Tang, J. M.; Flatte, M. E.; Yazdani, A. *Nature* **2006**, *442* (7101), 436−439.
(33) Marczinowski, F.; Wiebe, J.; Tang, J. M.; Flatte, M. E.; Meier, F.; Morgenstern, M.; Wiesendanger, R. *Phys. Rev. Lett.* **2007**, *99* (15), 157202.
(34) Schlaf, R.; Lang, O.; Pettenkofer, C.; Jaegermann, W. *J. Appl. Phys.* **1999**, *85* (5), 2732−2753.
(35) Hughes, H. P., Starnberg, H. I. *Electron Spectroscopies Applied to Low-Dimensional Structures*; Kluwer Academic Publishers: Dordrecht, the Netherlands, 2000.
(36) *Gmelin Handbook of Inorganic and Organometallic Chemistry*, 8th ed.; Springer-Verlag: Berlin, Germany, 1995; Vol. *B7*.
(37) Constant, I.; Tardif, F.; Derrien, J. *Semicond. Sci. Technol.* **2000**, *15* (1), 61.
(38) Luican-Mayer, A.; Kharitonov, M.; Li, G. H.; Lu, C. P.; Skachko, I.; Goncalves, A. M. B.; Watanabe, K.; Taniguchi, T.; Andrei, E. Y. *Phys. Rev. Lett.* **2014**, *112*, 036804.